Article

Human α-synuclein aggregation activates ferroptosis leading to parvalbumin interneuron degeneration and motor learning impairment

Check for updates

Borui Zhang[1,6], Kai Chen[1,6], Yelin Dai[1], Xi Luo[1], Ziwei Xiong[1,6], Weijia Zhang[1], Xiaodan Huang[1], Kwok-Fai So ®[1,2,3,4,5] & Li Zhang ®[1,3,4,5] ✉

The accumulation of α-synuclein induces neuronal loss in midbrain nuclei and leads to the disruption of motor circuits, while the pathology of α-synuclein in cortical regions remains elusive. To better characterize cortical synucleinopathy, here we generate a mouse model with the overexpression of human α-synuclein in the primary motor cortex (M1) of mice. A combination of molecular, in vivo recording, and behavioral approaches reveal that cortical expression of human α-synuclein results in the overexcitation of cortical pyramidal neurons (PNs), which are regulated by the decreased inhibitory inputs from parvalbumin-interneurons (PV-INs) to impair complex motor skill learning. Further mechanistic dissections reveal that human α-synuclein aggregation activates ferroptosis, contributing to PV-IN degeneration and motor circuit dysfunction. Taken together, the current study adds more knowledge to the emerging role and pathogenic mechanism of ferroptosis in neurodegenerative diseases.

The aggregation of α-synuclein is one of the major pathogenic factors in neurodegenerative disorders, including Parkinson's disease (PD) and Alzheimer's disease (AD)[1,2]. Current knowledge has identified synucleinopathy and neuronal loss in subcortical nuclei such as the substantia nigra compacta (SNc) in PD patients[3]. Such a model of midbrain dopaminergic circuit in PD pathogenesis, however, cannot fully explain motor syndromes. For example, limb rigidity and tremor were believed to be affected by the primary motor cortex (M1)[4], which regulates voluntary movement via local excitatory-inhibitory circuits and top-down projections. In human PD patients, cortical regions such as the cingulate cortex[5] also presented a higher abundance of α-synuclein oligomers. Besides PD, cortical α-synuclein deposits are also found in human Lewy body disease[6] and AD patients[7]. Therefore, further understanding of cortical synucleinopathy is critical for illustrating the pathology of neurodegenerative diseases.

Different theories have been proposed to explore the molecular mechanisms of neuronal degeneration under PD. The emerging model of lipid peroxidation and ferroptosis[8] has drawn research interest, as the potential role of ferroptosis in PD pathology has been reported[9,10]. In specific, potentiated ferroptosis has been found in both drug-induced[11] and transgenic PD models with α-synuclein overexpression[12]. The induction of ferroptosis may occur with the activation of neuroinflammation[13,14], contributing to neuronal death. The activation of microglial cells also resulted in the elevated release of chemokines release, further enhancing microglia migration[15]. As a consequence, microglia-mediated phagocytosis of synapse and neuronal soma disrupted neural networks[16,17]. These existing studies, however, mainly analyzed the ferroptosis in midbrain nuclei during PD pathogenesis[18], with insufficient focus on cortical regions.

In the current work, we generated a mouse synucleinopathy model by viral-mediated overexpression of the human α-synuclein (SNCA) gene into the M1. The de novo production of α-synuclein aggregates resulted in deficits of complex motor learning, in association with hyperactivation of cortical pyramidal neurons (PNs). Such overexcitation was found to be caused by the downregulation of parvalbumin-interneurons (PV-INs). Further molecular studies showed that following SNCA overexpression,

[1]Key Laboratory of CNS Regeneration (Ministry of Education), Guangdong-Hong Kong-Macau Institute of CNS Regeneration, Jinan University, Guangzhou, P. R. China. [2]State Key Laboratory of Brain and Cognitive Science, Li Ka Shing Faculty of Medicine, The University of Hong Kong, Hong Kong SAR, P. R. China. [3]Center for Brain Science and Brain-Inspired Intelligence, Guangdong-Hong Kong-Macao Greater Bay Area, Guangzhou, P. R. China. [4]Neuroscience and Neurorehabilitation Institute, University of Health and Rehabilitation Sciences, Qingdao, China. [5]Center for Exercise and Brain Science, School of Psychology, Shanghai University of Sport, Shanghai, China. [6]These authors contributed equally: Borui Zhang, Kai Chen, Ziwei Xiong. ✉e-mail: zhangli@jnu.edu.cn
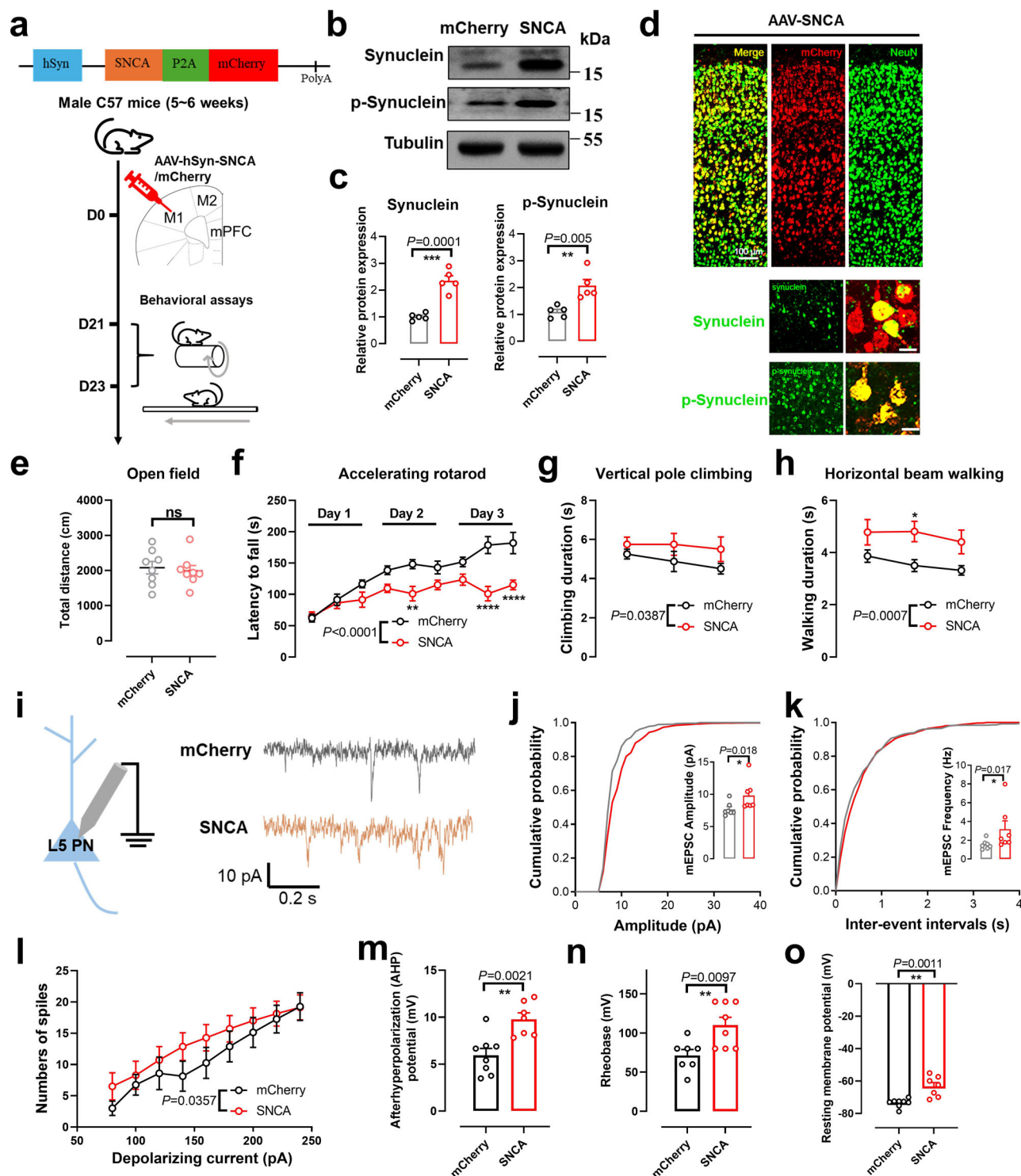
iron overload and disrupted ferroptosis probably caused cortical dysfunctions. In sum, our work revealed one previously unrecognized molecular pathway by which SNCA disrupts circuitry integrity and cortical function.

Results

SNCA overexpression in mouse M1 leads to cortical hyperexcitability and motor learning impairments

We first introduced SNCA-coding gene into the bilateral M1 of adult male mice using an adeno-associated virus (AAV) vector (Fig. 1a). Three weeks later, these mice presented significantly elevated levels of α-synuclein in M1 extracts ($P < 0.001$; Fig. 1b, c, Supplementary Fig. 1). In specific, phosphorylated α-synuclein proteins in neurons (NeuN+) can be found across different layers of M1 (Fig. 1d) as well as in axonal fibers from M1 to the dorsal striatum (DS) (Supplementary Fig. 2a). However, the postsynaptic neurons in DS did not exhibit transmission of protein aggregations, nor did other cortical regions (Supplementary Fig. 2a), thus suggesting M1-specificity of SNCA overexpression. In behavioral phenotyping, SNCA mice displayed normal anxiety levels or novel object recognition function ($P > 0.05$; Supplementary Fig. 2b–d). When examining the motor functions, SNCA mice had unchanged general motor ability ($P > 0.05$; Fig. 1e), whilst

Fig. 1 | Human α-synuclein resulted in motor learning deficits associated with cortical hyperexcitability. a Upper, the design of adeno-associated virus (AAV)-human synapsin (hSyn)-human α-synuclein (SNCA)-mCherry viral vector. Lower, Schematic diagram of generating mouse synucleinopathy model by expressing SNCA gene into bilateral primary motor cortex (M1) of adult male mice under the help of an AAV vector carrying hSyn promoter. Three weeks later, behavioral test batteries were performed. **b** Representative blotting bands of total synuclein and phosphorylated synuclein in M1 extracts. **c** Quantification for the relative expression of total (left) and phosphorylated synuclein (right). Two-sample unpaired t-test, $t(8) = 6.967$, $P = 0.0001$ for synuclein; $t(8) = 3.907$, $P = 0.005$ for p-synuclein. $N = 5$ mice in each group. **d** Upper panels: coronal section of mouse M1 after SNCA overexpression. AAV-SNCA was mostly expressed within neurons (NeuN+). Lower panels: cortical expression of synuclein and phosphorylated synuclein were observed. Scale bar, 100 μm or 20 μm (enlarged panels in lower right). **e** Total distance traveled in the open field arena was unaffected after SNCA overexpression. Two-sample unpaired t-test, $t(14) = 0.3807$, $P = 0.7091$. **f** SNCA-overexpressing mice had remarkably impaired motor performance on the accelerating rotarod. Two-way analysis of variance (ANOVA) with respect to group factor, $F(1126) = 55.81$, $P < 0.0001$. Sidak's multiple comparison test of post hoc comparison at each time point. **g** SNCA group spent longer time to accomplish the vertical climbing task. Two-way ANOVA with respect to group factor, $F(142) = 4.553$, $P = 0.0387$. Sidak's multiple comparison test of post hoc comparison at each time point. **h** Worsening performance on the walking beam in mutant mice. $F(139) = 13.55$, $P = 0.0007$. Sidak's multiple comparison test of post hoc comparison at each time point. $N = 8$ mice in each group in (**e**–**h**). **i** Patch-clamp recording traces of layer 5 pyramidal neurons (L5 PNs) showed potentiated miniature excitatory postsynaptic currents (mEPSCs) in SNCA group. **j** SNCA group had higher amplitude of mEPSCs. Non-parametric Mann–Whitney test $U = 6$, $P = 0.018$. **k** Increased frequency of mEPSCs was observed under synucleinopathy. Non-parametric Mann–Whitney test $U = 6$, $P = 0.017$. **l** Elevated number of action potentials (AP) in SNCA group under fixed injection currents. Two-way ANOVA with respect to group factor, $F(1104) = 4.530$, $P = 0.0357$. **m** Higher potentials of afterhyperpolarization (AHP). Two-sample unpaired t-test, $t(13) = 3.817$, $P = 0.0021$. **n** Higher rheobase values in SNCA group. Two-sample unpaired t-test, $t(13) = 3.026$, $P = 0.0097$. **o** Decreased resting membrane potential (RMP) in SNCA group. Two-sample unpaired t-test, $t(13) = 4.181$, $P = 0.0011$. $N = 8$ and 7 neurons from 3 animals in mCherry and SNCA group, respectively, in (**j**–**o**). ns, no significant difference, $*P < 0.05$, $**P < 0.01$, $***P < 0.001$, $****P < 0.0001$. All data were presented as mean ± SEM.

their abilities to acquire complex motor skills were disrupted. Of note, SNCA mice presented similar latency on the accelerating rotarod compared to control groups during the initial trial, whilst their performance did not improve with repeated training sessions ($P < 0.0001$; Fig. 1f). In a similar manner, SNCA mice had longer duration in accomplishing vertical climbing or horizontal beam walking task ($P < 0.05$; Fig. 1g, h). These data suggested that SNCA accumulation in the motor cortex resulted in dysregulated motor learning functions.

Cortical neuronal activity is closely associated with motor learning functions, and hyperexcitability of the cortex has been reported in neurodegenerative diseases[19,20]. To investigate the cortical neural network homeostasis, we employed ex vivo whole-cell patch-clamp recording on acute M1 slices. SNCA mice had potentiated miniature excitatory postsynaptic currents (mEPSCs; Fig. 1i) of layer 5 pyramidal neurons (L5 PNs). In specific, both the amplitude and frequency of mEPSCs were elevated ($P < 0.05$; Fig. 1j, k). Such observations of higher synaptic transmission paralleled with the potentiated membrane excitability in SNCA group, including more frequent action potential spikes ($P < 0.05$; Fig. 1l), plus higher values of afterhyperpolarization (AHP), Rheobase and resting membrane potential (RMP) ($P < 0.01$, Fig. 1m–o).

The disruption of synaptic functions indicated the dysregulation of the cortico-striatal pathway, which was closely associated with complex motor skills[21]. To further support this hypothesis, we performed in vivo calcium imaging of M1 by co-expressing genetically encoded calcium indicator GCaMP6s along with SNCA (Fig. 2a). Three weeks later, the calcium transient of L5 PNs was recorded on awake, head-fixed mice (Fig. 2b). SNCA mice displayed higher total integrated calcium activities ($P < 0.001$; Fig. 2c), which can be attributed to the higher frequency of calcium spikes ($P < 0.001$; Fig. 2d). To investigate the downstream projecting region of M1, we utilized the in vivo fiber photometry to record the calcium activity of cortical PN fibers within the dorsal striatum (DS) while the mouse was trained on the rotarod (Fig. 2e, f). A major calcium peak occurred when the animal fell down from the rod (Fig. 2g). The strength of this calcium episode, however, was remarkably increased in the SNCA group ($P < 0.05$; Fig. 2g–i). These results paralleled the hyperexcitability of cortical PNs (Fig. 2b–d) and suggested that cortical overexpression of SNCA resulted in motor learning deficits, which was correlated with hyperexcitation of the cortico-striatal pathway.

Disrupted cortical excitatory-inhibitory balance underlies SNCA-induced motor learning deficits

The excitatory-inhibitory (E/I) balance of the cortical neural network is critical for maintaining normal functions. We thus tested the role of cortical E/I balance in motor learning deficits in SNCA-overexpressed mice. The

first piece of evidence came from expressing the designer receptors exclusively activated by designer drugs (DREADD) hM4Di along with AAV-SNCA into mouse M1 (Supplementary Fig. 3a). Chronic infusion of specific ligand clozapine-N-oxide (CNO) remarkably improved motor learning functions ($P < 0.01$; Supplementary Fig. 3b–d), suggesting the participation of cortical hyperexcitation underlying motor learning deficits of SNCA model. To dissect the circuitry mechanism, local PV-INs were further studied as they innervate cortical PNs to exert indispensable functions in motor learning[22]. Via immunofluorescent staining, we identified remarkably decreased expression of PV-INs across different M1 layers ($P < 0.001$; Fig. 3a, b), plus the loss of perineuronal nets (PNNs) which coat PV-INs using wisteria floribunda agglutinin (WFA) as the marker ($P < 0.001$; Fig. 3c). In addition, we found that only PV-INs showed decreased density under SNCA, but not for vasoactive intestinal peptide (VIP) or somatostatin (SST) interneurons (Supplementary Fig. 4), supporting the subtype-specific effect. To recapitulate such cellular pathology, Cre-dependent Caspase 3 was expressed into M1 of PV-IRES-Cre mice (Supplementary Fig. 5a), leading to decreased density of PV-INs ($P < 0.001$; Supplementary Fig. 5b, c) and motor learning deficits ($P < 0.05$; Supplementary Fig. 5d–f) as those in SNCA-overexpressed mice. These data supported the correlation between motor dysfunction and PV-IN loss under synuclein overexpression.

Subsequently, the calcium activity of PV-INs was recorded by in vivo 2-photon microscopy (Fig. 3d). SNCA mice displayed a decreased frequency of calcium transients of PV-INs, resulting in lower total calcium activities (Fig. 3e–g). The depressed inhibitory transmission might contribute to the overexcitation of L5 PNs, which receive GABAergic innervations from PV-INs. To provide the direct causal relationship, we then used a chemogenetic approach to selectively activate cortical PV-INs by expressing excitatory receptor hM3Dq into PV-INs along with AAV-SNCA (Fig. 3h). Chronic CNO infusion significantly elevated cortical neuronal activities ($P < 0.001$; Fig. 3i, j). Furthermore, behavioral phenotyping showed remarkable improvements in the accelerating rotarod test ($P < 0.0001$; Fig. 3k), as well as the vertical pole climbing ($P < 0.0001$; Fig. 3l) or horizontal beam walking task ($P < 0.0001$; Fig. 3m). Taken together, α-synuclein impaired cortical E/I balance via suppressing PV-INs, leading to motor learning deficits.

Microglia activation impairs cortical circuits to disrupt motor learning

Under SNCA overexpression, microglia is the primary cell type for extracellular protein aggregates clearance[23], during which both morphological and molecular features of microglia are prominently altered. We thus used ionized calcium-binding adapter molecule 1 (Iba1) as the cellular marker to study the morphology of cortical microglia (Fig. 4a).
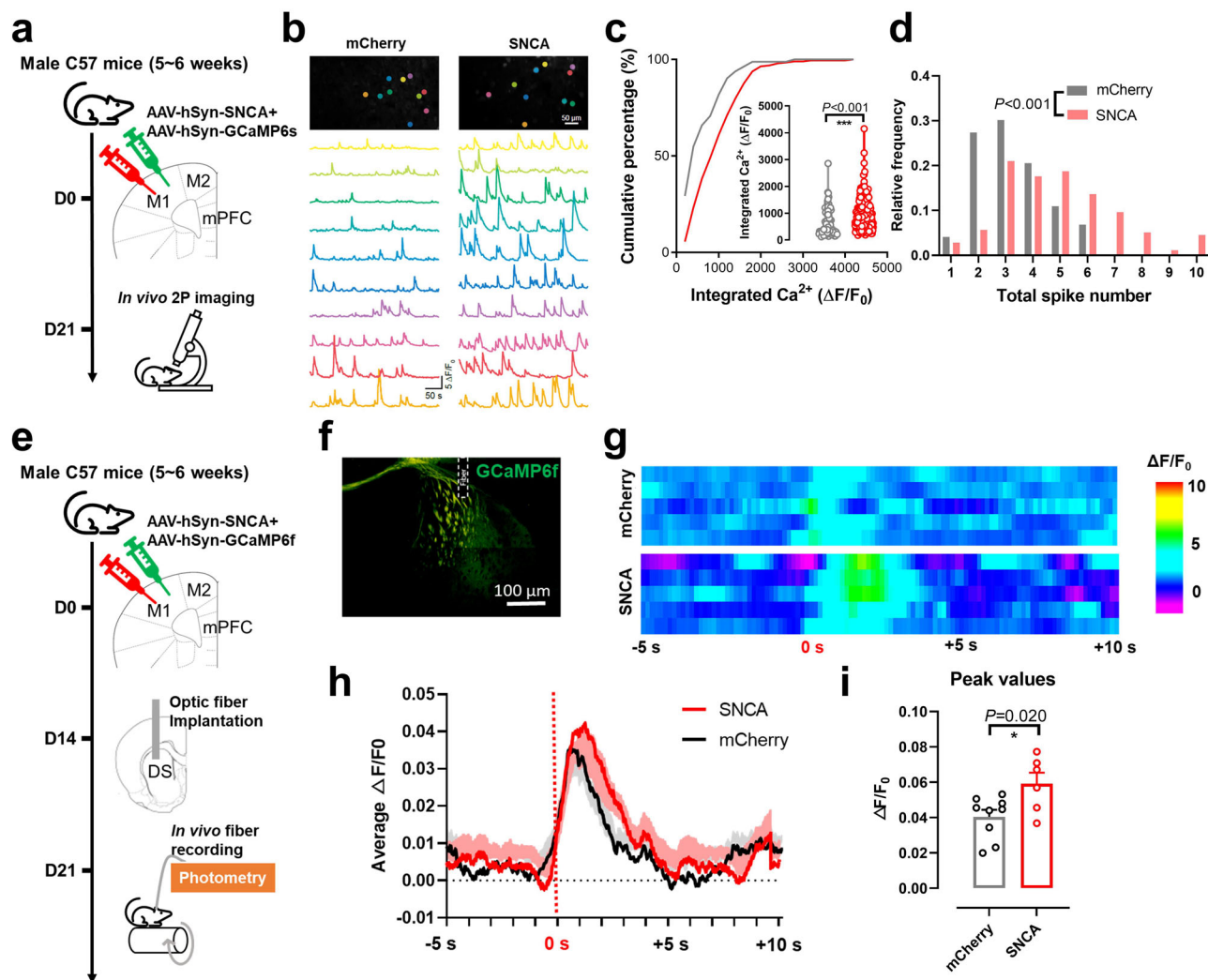
Fig. 2 | Dysregulated cortico-striatal pathway under SNCA. a Illustrations for the in vivo two-photon microscopy assay, in which one single imaging session was performed at 3 weeks after co-expressing GCaMP6s and SNCA into M1. **b** Sampled field of views (FOVs) from each group, with sample traces of calcium transients, were listed for each color-coded neuron. The calcium signal was calculated as $\Delta F/F_0$. Scale bar, 50 μm. **c** SNCA-overexpressed mice had remarkably higher total calcium transients. Non-parametric Kolmogorov–Smirnov test, D = 0.3749, $P < 0.001$. **d** Model mice showed higher frequency of calcium spikes. D = 0.3503, $P < 0.001$. $n = 82$ and 196 cells from 4 mice of mCherry and SNCA group, respectively, in (**c, d**). **e** Experimental design of fiber photometry recording of PN-DS terminus. At 14 days after infecting M1 with GCaMP6f, an optic fiber was implanted into DS. One week later, the calcium activity within DS was recorded when the mouse was trained on the accelerating rotarod. **f** Fiber implantation and GCaMP6s infection sites within DS. Scale bar, 100 μm. **g** Heatmaps for the normalized calcium activities (in $\Delta F/F_0$) during the motor task. A major peak occurred when the mouse fell down from the rod ($t = 0$ s). **h** Averaged calcium values from 20 trials. **i** Quantification of peak calcium values found potentiated signal strength in SNCA group. Two-sample unpaired t-test, $t(13) = 2.640$, $P = 0.020$. $N = 9$ and 6 mice from mCherry and SNCA groups, respectively. $*P < 0.05$, $***P < 0.001$. All data were presented as mean ± SEM.

In SNCA-overexpressing mice, microglia presented elevated cell density and phagocytosis toward SNCA-expressing cells ($P = 0.011$; Fig. 4a, b), in association with higher Iba1 and CD68 expressions ($P = 0.037$; Fig. 4c, d, Supplementary Fig. 6). The morphometric study of individual microglial cells further revealed enlarged soma size ($P < 0.001$; Fig. 4e, f) and highly branched processes ($P < 0.001$; Fig. 4g), suggesting the activation of cortical microglia upon SNCA overexpression.

To validate the role of microglia activation in cortical dysfunction, we employed PLX5622, one potent inhibitor of colony-stimulating factor 1 receptor (CSFR1), to suppress the microglial population[24]. By feeding mice with PLX5622-contained food chows (Fig. 4h), we successfully eliminated the majority of cortical microglial cells ($P < 0.001$; Fig. 4i, j). Of note, the number of PV-INs was also recovered by microglial ablation ($P < 0.001$; Fig. 4i, k). Further motor learning tasks revealed the remarkable improvement of motor learning deficits of SNCA mice after microglial inhibition ($P < 0.01$; Fig. 4l–n). These data highlighted the role of activated microglia in synucleinopathy-related motor learning deficits.

## Disruption of ferroptosis mediates cortical PV-INs loss and motor learning dysfunctions

Although we have observed the contribution of microglial activation in cortical deficits under SNCA overexpression, the detailed molecular mechanism remained unclear. We thus employed a transcriptomic study of mouse M1 extracts to investigate the differentially regulated genes (DEGs). Bioinformatics analysis identified a total of 157 up-regulated and 115 down-regulated genes in SNCA mice (Supplementary Fig. 7). Using the Kyoto Encyclopedia of Genes and Genomes (KEGG) database, the ferroptosis pathway was found to be prominently affected (Fig. 5a). Previous knowledge recognized ferroptosis to be involved in the molecular pathology of neurodegenerative diseases[8,25]. The quantification of gene transcript expression level in M1 found upregulation of ferroptosis-related genes such as Phospholipase A2 group VI (*Pla2g6*), cystine/glutamate antiporter solute carrier family 7 member 11 (*Slc7a11*), prostaglandin-endoperoxide synthase 2 (*Ptgs2*) and transferrin receptor (*Tfrc*) ($P < 0.05$; Fig. 5b), supporting the activation of ferroptosis in SNCA group.
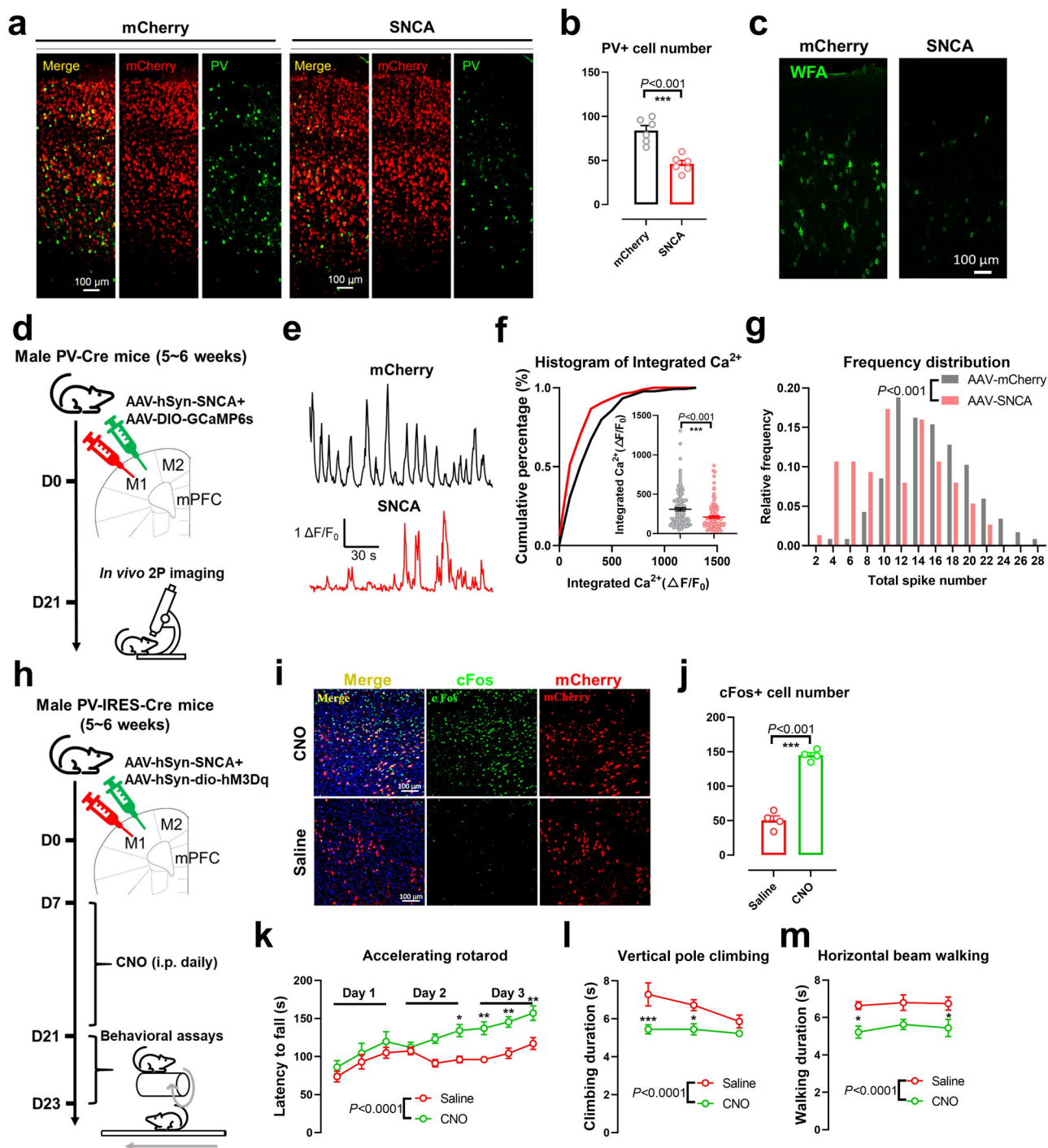
Fig. 3 | Parvalbumin-interneurons mediate SNCA-associated motor learning deficits. a Coronal sections of mouse M1 for SNCA expression and parvalbumin-interneurons (PV-INs). Scale bar, 100 μm. **b** SNCA-overexpressed mice had remarkably decreased density of PV-INs. Two-sample unpaired t-test, $t(10) = 5.491$, $P = 0.0003$. $N = 6$ mice in each group. **c** Fluorescent staining for the wisteria floribunda agglutinin (WFA) as the marker of perineuronal nets around PV-INs. Scale bar, 100 μm. **d** Experimental design for in vivo calcium recording of PV-INs via Cre-mediated GCaMP6s expression on PV-Cre mice. **e** Sample traces of calcium transients of PV-INs from both groups. **f** Comparison of total integrated calcium signal strength showed decreased activities in the SNCA group. Non-parametric Kolmogorov–Smirnov test, D = 0.2557, $P = 0.0009$. **g** The frequency of calcium transients was also depressed in the model group. Non-parametric Kolmogorov–Smirnov test, D = 0.3480, $P < 0.0001$. $n = 134$ and 105 neurons from 4 mice of mCherry and SNCA groups, respectively, in (**f, g**). **h** Illustration for experimental procedures of rescuing assay, in which excitatory hM3Dq under

Cre-dependent expression was introduced into PV-IRES-Cre mice, followed by 2-week CNO administration and motor learning phenotyping. **i** Representative immunofluorescent staining for cFos activity. Scale bar, 100 μm. **j** cFos activity was reduced by CNO treatment. Two-sample unpaired t-test, $t(6) = 12.52$, $P < 0.0001$. $N = 4$ mice in each group. **k** Chemogenetic activation of cortical PV-INs improved motor learning abilities on the rotarod. Two-way ANOVA with respect to group factor, $F(1126) = 43.38$, $P < 0.0001$. Sidak's multiple comparison test of post hoc comparison at each time point. **l** PV-INs excitation conferred better performance on vertical pole climbing. Two-way ANOVA with respect to group factor, $F(142) = 21.66$, $P < 0.0001$. Sidak's multiple comparison test of post hoc comparison at each time point. **m** The reaction of PV-INs also enhanced the acquisition of beam walking abilities. $F(142) = 19.78$, $P < 0.0001$. Sidak's multiple comparison test of post hoc comparison at each time point. $N = 7$ and 9 mice in saline and CNO group, respectively, in (**k–m**). ***$P < 0.001$. All data were presented as mean ± SEM.
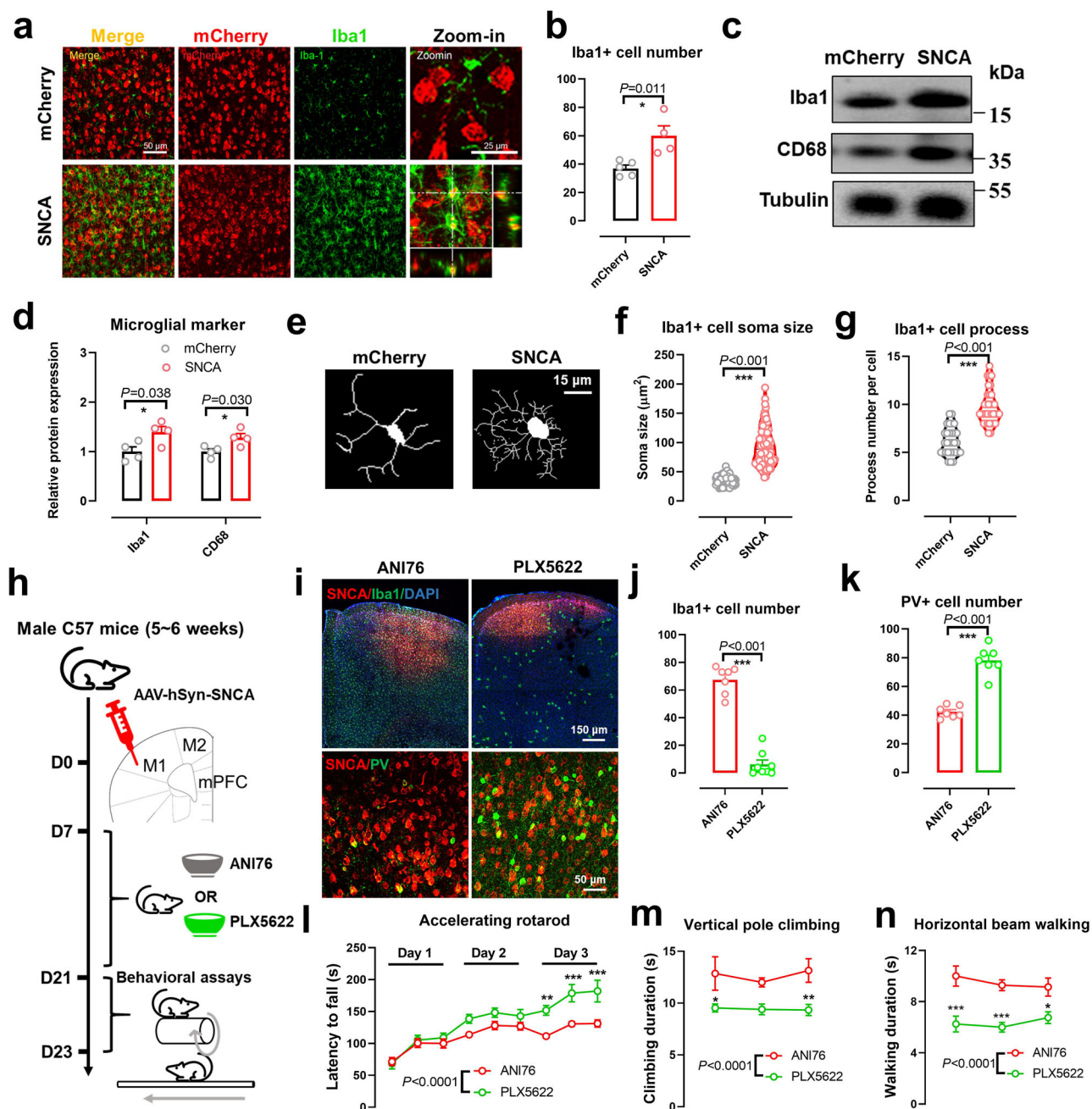
Fig. 4 | Reactive microglia mediate PV-INs depopulation to impair motor behaviors. a Immunofluorescent staining of microglial cells (Iba1+) and its phagocytosis toward SNCA-expressing cells (mCherry labeled) in M1 from SNCA model mice. Scale bare, 50 μm or 25 μm (enlarged views only). **b** The number of microglial cells in the given field was increased by SNCA overexpression. Two-sample unpaired *t*-test, t(7) = 3.419, P = 0.0112. N = 5 and 4 mice from mCherry and SNCA group, respectively. **c** Representative blotting bands of Iba1 and CD68 from M1 extracts. **d** Quantification of relative protein expression of Iba1 and CD68. Multiple *t*-test showed significant difference between groups. P = 0.038 for Iba1 and P = 0.030 for CD68. N = 4 mice in each group. **e** Contours of sampled microglial morphology. Scale bar, 15 μm. **f** Microglial cells of model mice also had larger soma size compared to control group. D = 0.9420, P < 0.0001. **g** SNCA model mice presented more cell processes of microglia on average. Non-parametric Kolmogorov–Smirnov test, D = 0.7429, P < 0.0001, n = 30 and 35 cells from 4 mice in each group, in (**f, g**). **h** Graphic illustration of microglial ablation assays. SNCA-overexpressed mice were fed with PLX5622-containing food chows for 2 weeks, in contrast with a control group receiving normal (ANI76) diet. Behavioral

phenotyping was performed later. **i** Representative immunofluorescent staining images of microglial cells and PV-INs. Although PLX5622 did not change the level of α-synuclein, PV-IN population was maintained. Scale bar, 150 μm in upper panels and 50 μm in lower panels. **j** Oral PLX5622 administration remarkably decreased microglial cell density. Two-sample unpaired *t*-test, t(13) = 12.61, P < 0.001. **k** Ablation of microglial cells increased PV-INs density. t(13) = 9.071, P < 0.001. N = 7 and 8 mice in ANI76 and PLX5622 group, respectively, in (**j, k**). **l** PLX5622 treatment recovered mouse performance on the accelerating rotarod. Two-way ANOVA with respect to group factor, F(1117) = 34.80, P < 0.0001. Sidak's multiple comparison test of post hoc comparison at each time point. **m** Microglia ablation improved the performance on vertical pole climbing task. Two-way ANOVA with respect to group factor, F(139) = 21.88, P < 0.0001. Sidak's multiple comparison test of post hoc comparison at each time point. **n** PLX5622 intervention rescued impairment on the walking beam. F(1,39) = 45.28, P < 0.0001. Sidak's multiple comparison test of post hoc comparison at each time point. N = 7 and 8 mice from ANI76 and PLX5622 group, respectively, in (**l–n**). *P < 0.05, **P < 0.01, ***P < 0.001. All data were presented as mean ± SEM.
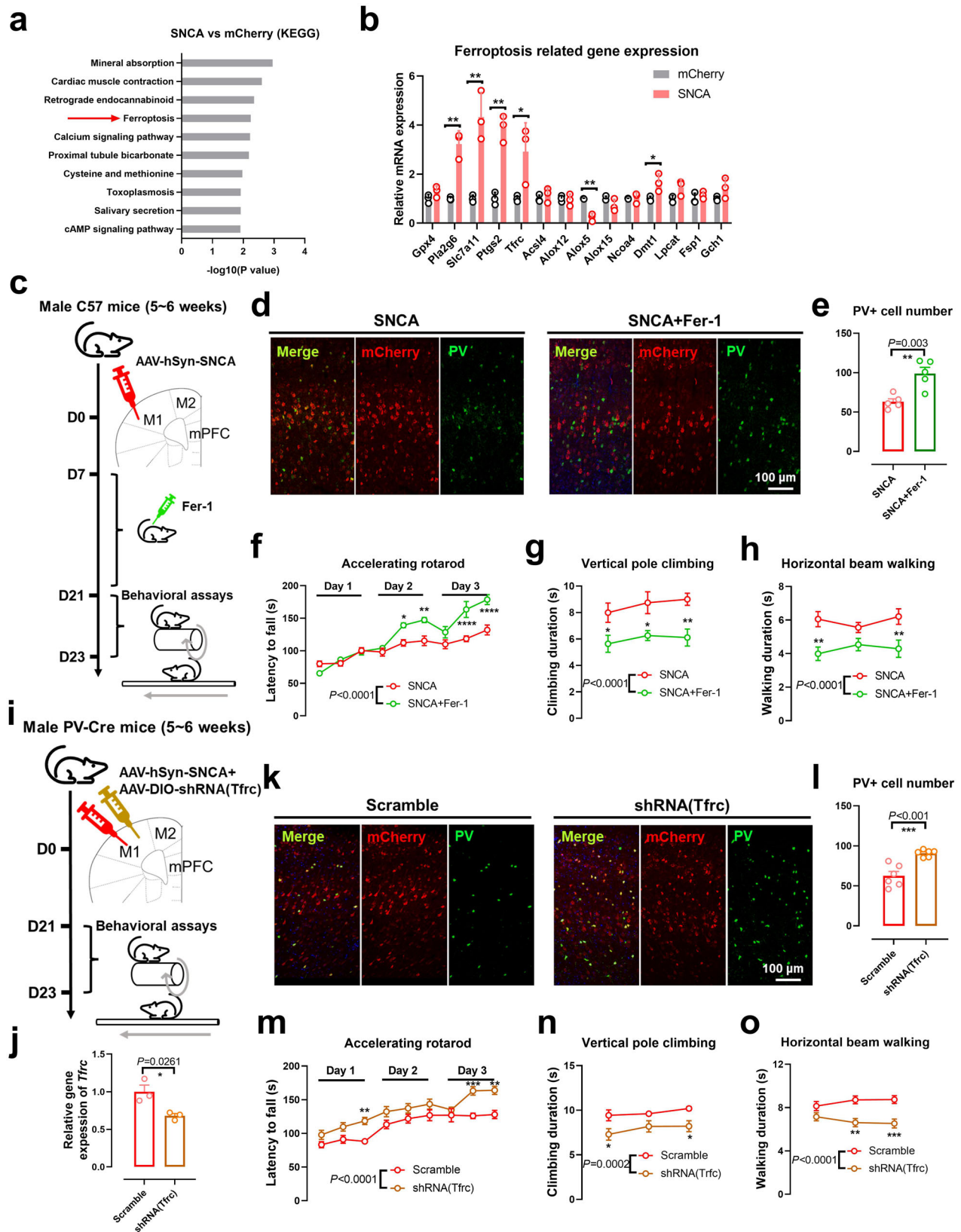
To substantiate the role of ferroptosis in SNCA-induced cortical pathology, the potent inhibitor of ferroptosis, ferrostatin-1 (Fer-1)[26] was infused into SNCA model mice (Fig. 5c). Fourteen-day drug treatment remarkably recovered normal PV population density in M1 ($P = 0.003$; Fig. 5d, e) and rescued impairments of complex motor skill learning ($P < 0.0001$; Fig. 5f–h). As Fer-1 mainly targets the excess free oxidative radicals in the presence of iron[26], an alternative approach was performed via short hairpin RNA (shRNA)-mediated silencing of *Tfrc* gene expression selectively in PV-INs to manipulate the intracellular trafficking of iron (Fig. 5i, j). Morphometric studies revealed that PV-IN population was

Fig. 5 | SNCA mediates iron homeostasis and the ferroptosis pathway for PV-INs loss. a Kyoto Encyclopedia of Genes and Genomes (KEGG) analysis for the differentially regulated pathways of SNCA group. **b** Relative gene expression levels of major factors in the ferroptosis pathway. Multiple t-tests were used. $P = 0.0021$, 0.0047, 0.0012, 0.0490, 0.0010, and 0.0406 for *Pla2g6*, *Slc7a11*, *Ptgs2*, *Tfrc*, *Alox5*, and *Dmt1* gene, respectively. $N = 3$ mice in each group. **c** Graphic illustration of ferroptosis inhibition assay using ferrostatin-1 (Fer-1) administration for 2 weeks on SNCA model. **d** Representative immunofluorescent staining for SNCA-expression (mCherry) and PV-INs population. Scale bar, 100 μm. **e** Fer-1 treatment remarkably increased PV-INs density. Two-sample unpaired t-test, $t(8) = 4.146$, $P = 0.0032$. $N = 5$ mice per group. **f** Blockade of ferroptosis significantly improved mouse performance on the accelerating rotarod. Two-way ANOVA concerning group factor, $F(1,90) = 41.67$, $P < 0.0001$. Sidak's multiple comparison test of post hoc comparison at each time point. **g** Fer-1 treatment enhanced the mouse performance on the vertical pole climbing task. Two-way ANOVA concerning group factor, $F(130) = 25.03$, $P < 0.0001$. Sidak's multiple comparison test of post hoc comparison at each time point. **h** Under Fer-1 infusion, the ability to finish the walking beam take was improved. Two-way ANOVA concerning group factor, $F(130) = 23.67$,

$P < 0.0001$. Sidak's multiple comparison test of post hoc comparison at each time point. $N = 6$ mice per group in (**f–h**). **i** Experimental design of iron uptake inhibition assay using shRNA-based silencing of *Tfrc* gene on SNCA model. **j** Relative expression of *Tfrc* gene after shRNA expression. Two-sample unpaired t-test, $t(4) = 3.449$, $P = 0.0261$. $N = 3$ mice per group. **k** Representative immunofluorescent staining for SNCA-expression (mCherry) and PV-INs population. Scale bar, 100 μm. **l** *Tfrc* gene knockdown significantly recovered the PV-INs population. Two-sample unpaired t-test, $t(10) = 4.849$, $P = 0.0007$. **m** Blockade of cellular iron uptake significantly improved the mouse performance on the accelerating rotarod. Two-way ANOVA concerning group effect, $F(199) = 52.80$, $P < 0.0001$. Sidak's multiple comparison test of post hoc comparison at each time point. **n** The silencing of the *Tfrc* gene improved the mouse performance on vertical pole climbing tasks. Two-way ANOVA concerning group factor, $F(130) = 18.74$, $P = 0.0002$. Sidak's multiple comparison test of post hoc comparison at each time point. **o** Under *Tfrc* gene deficiency, the ability to finish the walking beam take was improved. $F(130) = 31.66$, $P < 0.0001$. Sidak's multiple comparison test of post hoc comparison at each time point. $N = 6$ mice per group in (**l–o**). *$P < 0.05$, **$P < 0.01$, ***$P < 0.001$. All data were presented as mean ± SEM.

increased after iron transport was blocked ($P < 0.001$; Fig. 5k–l). Moreover, the skill of complex motor functions was remarkably improved with the deprivation of *Tfrc* gene in PV-INs ($P < 0.001$; Fig. 5m–o) as those of Fer-1 treated animals. Due to the unaffected microglial cell population in DS after SNCA overexpression (Supplementary Fig. 8a), and similar microglial density under either Fer-1 or shRNA (*Tfrc*) treatment (Supplementary Fig. 8b, c), it is likely that SNCA overexpression in M1 only leads to local neuroinflammatory response, and ferroptosis acts at the downstream of neuroinflammation to confer cellular toxicity to PV-INs. Taken together, our molecular, physiological, and behavioral data supported the role of ferroptosis in mediating PV-INs depopulation and cortical dysfunction, under local overexpression of SNCA.

Discussion

The current study revealed the previously unrecognized role of disrupted E/I balance in cortical regions following α-synuclein aggregation. Cortical inhibitory neurons are critical for maintaining normal neural functions, and the dysregulation of INs may result in neurological disorders. Of note, our work suggested potentially suppressed presynaptic inhibitory inputs towards PNs, leading to the overexcitation of cortico-striatal pathway and motor learning deficits. These results thus illustrated the changes of cortical circuits under SNCA overexpression, providing the neural mechanism for motor learning deficits. As further molecular evidence, iron overload and ferroptosis are believed to be involved in cortical E/I imbalance.

The region- and cell-type-specific expression of α-synuclein is one critical issue for illustrating the circuitry mechanism of PD. Current studies mainly focused on dopaminergic neurons whilst leaving the GABAergic cells largely unattended. Some comparative studies in mouse tissues found the co-existence between α-synuclein and vesicular glutamate transporter 1 (vGluT1) but not in cortical GABAergic neurons under normal conditions[27,28]. The exogenous supply of SNCA fibrils induced intracellular aggregation formation in inhibitory neurons, which did not present the formation of Lewy body structure as those in excitatory neurons[28]. These results highlighted the potentially differentially regulated pathway for synucleinopathy in inhibitory neurons. In our model, SNCA was expressed in both glutamatergic and GABAergic cells, the latter of which presented cell loss in the first place. It is worth noticing that the downregulation of PV-INs has been found across different neurological disorders, including autism[29], PD[30] and AD[31]. Although no direct evidence has been obtained to demonstrate the neuronal loss of PV-INs in our work, and reports from PD patients did not reveal the neuronal degeneration in cortical regions[32], a few models have been discussed to explain the vulnerability of GABAergic neurons under proteinopathy, including the relatively higher energy requirement[33], or the preference of microglial phagocytosis targeting the extracellular matrix of PV-INs[34].

GABAergic INs play indispensable roles in maintaining the structural and functional integrity of cortical circuits. PV-INs are the major subtype of

inhibitory cells forming peri-somatic innervations of PNs to exert rapid and powerful inhibition[35], providing critical inputs for maintaining the E/I balance of the cortical network[36]. From functional perspectives, cortical PV-INs have been found to regulate social behaviors[37], sensory integration[38,39] and spatial working memory[40]. The disruption of normal PV-IN function resulted in mental disorders such as schizophrenia[41]. In motor cortex, PV-INs work with other INs to shape task-dependent ramping signals preceding motor movements[42] and help to regulate the plasticity of other inhibitory boutons during rotarod motor learning[43]. Our data illustrated the participation of PV-INs in tuning the calcium activity of PNs, as cell-specific ablation and chemogenetic excitation effectively recapitulated or reversed SNCA-induced hyperexcitability of local L5 PNs, respectively. These results highlighted the importance of cortical E/I balance in executing normal motor learning tasks. Since inhibitory transmission can be regulated by noninvasive neuromodulation approaches such as transcranial magnetic stimulation (TMS)[44], strategies might be developed to target cortical inhibitory network for the alleviation of Parkinsonism.

In searching for the molecular mechanism governing the gradual loss of PV-INs upon SNCA overexpression, we proposed that ferroptosis signaling might be related to PV-INs loss. In the current work, we found prominent changes in ferroptosis-related genes, including *Pla2g6*, *Slc7a11*, *Ptgs2*, and *Tfrc*. To further demonstrate the participation of this ferroptosis pathway, the pharmaceutical inhibitor Fer-1 was employed to rescue PV-IN degeneration and motor learning deficits. Moreover, the involvement of iron homeostasis was supported via depressing *Tfrc* gene expression, in order to inhibit cellular iron uptake for relieving iron overload. The excess iron content may further disrupt the catabolism of lipid peroxide, leading to the activation of the ferroptosis cascade in cortical neurons, as supported by a recent study using the spinal injury model[45]. Since ferroptosis in the striatum might be related to intracerebral hemorrhage[46] and PD[47], the targeting of ferroptosis may provide a potential strategy for PD treatment.

The activation of the ferroptosis pathway is closely related to PD pathogenesis. Amounts of studies have supported the participation of iron overload and the disruption of critical regulators of the ferroptosis pathway during PD pathogenesis. For example, in a homozygous PD mouse model (α-Synuclein A53T mutant), dopaminergic neuronal death is caused by iron overload during the early disease stage[48]. The iron overload also induced the transcriptomic dynamic shift of PD patients' brains toward ferroptosis, as supported by the human-induced pluripotent stem cell-derived microglial cell culture assay[49]. In a drug-induced PD model, iron accumulation and ferroptosis were also reported, in addition to the rescued phenotype by Fer-1 treatment[50] similar to our work. Moreover, a recent study using dopaminergic cell culture model further supported the protective role of Ferritin against neurotoxicity[51]. These in vitro and in vivo data all agreed on the relationship between iron overload in conjunction with ferroptosis and PD susceptibility and proposed the potential value of targeting the ferroptosis pathway for

neuroprotection. Although these abovementioned works mainly studied midbrain dopaminergic neurons, here we presented amounts of data showing the critical role of this pathway in cortical neuronal functions. More importantly, by specifically modulating *Tfrc* gene expression in PV-INs, we reported the necessary role of ferroptosis in cortical INs under synucleinopathy.

In sum, SNCA disrupted E/I balance of the motor cortex, mainly due to the downregulation of PV-INs, which leads to the hyperexcitation of PNs and motor learning deficits. The loss of PV-INs was potentially related to microglial activation and elevated ferroptosis. Our work provides more mechanisms for neuropathology under synucleinopathy and implies potential molecular and circuitry targets for future interventional strategies.

Methods

Experimental animals
C57BL/6J mice (5 weeks old, male) were purchased from Guangdong Medical Laboratory Animal Center. PV-Cre mice (5 weeks old, male) were obtained from Jackson Laboratory and were bred by Shanghai Model Organisms Center, Inc. Unless otherwise specified, all mice were group housed (4–5 individuals per standard cage) with food and water ad libitum. The animal facility was kept with a 12 h light/dark cycle (light 8:00–20:00, dark 20:00–8:00), and the temperature was maintained at 24 ± 2 °C, with the relative humidity at 50 ± 10%. All animal experimental protocols have been approved by the Ethics Committee of Experimental Animals of Jinan University in accordance with Institutional Animal Care and Use Committee guidelines for animal research.

For PLX5622 treatment, 0.12% PLX5622 was prepared in standard AIN-76A rodent diet, which was provided by Dyets Inc. Mice were provided PLX5622-containing chow starting at 7 days after virus infection. For Fer-1 treatment, mice received intraperitoneal injection of Fer-1 (MedChemExpress, US) at 5 mg/kg for 14 consecutive days.

Stereotaxic injection and two-photon imaging
Mice were anesthetized with 1.25% Avertin. After local sterilization and incision of head skins, the primary motor cortex (M1, AP: +0.5 mm anterior to the Bregma; ML: ±1.2 mm lateral; and DV: −0.6 mm depth) was located under a stereotaxic instrument (RWD Life Science, China). After drilling a hole with the high-speed microdrill (WPI, USA), 100 nl of AAV serotype 2/9 (viral titer, 5×10^{12} genome copies per ml, see Supplementary Table 1) was injected using a glass micropipette connected to an ultra-micro injection pump (Nanoliter 2020, WPI, USA). The glass electrode was retained within the brain tissue for 8 min before retraction. After the virus injection, the scalp was sutured, and the mouse was placed back in the cage for 1-week recovery. Analgesics (buprenorphine at 0.1 mg/kg) was used when necessary.

One day before the imaging session, a transcranial imaging window was prepared. In brief, the head skin and the skull over the primary motor cortex were carefully removed by a microdrill. The window was covered by a glass coverslip using Tissue Adhesive (3M, USA). The imaging session was recorded at 2 Hz using a 920 nm excitation laser with a water-immersed objective (20×; ZEISS, Germany) under an LSM780 two-photon microscope (ZEISS, Germany).

Acquired images were analyzed by ImageJ (NIH, US). The fluorescent value was quantified from the designed region of identifiable soma. The $\triangle F/F_0$ was calculated as $(F − F_0)/F_0$, where the F_0 was the minimum of F values as the basal level. A calcium spike was defined when the $\triangle F/F_0$ was higher than three-fold standard deviations (SDs).

Behavioral assays
Open field. The test apparatus contained a transparent field at 50 × 50 × 50 cm, with an arbitrary defined central area (25 × 25 cm). During the 5-min single test session, the Ethovison XT software was used to track and analyze the mouse movement trajectory. The anxiety level was evaluated using the time in the central area.

Novel object recognition task. The experiment procedure followed our previous works[52]. In brief, the animal's preference toward a novel object was evaluated by the exploration time during 10 min test session, which was carried at 15 min or 24 h after the initial learning session (10 min, including 2 identical objects). The Ethovison XT software was used to record and analyze the movement trajectories.

Accelerating rotarod test. The Rotarod system (UGO Basile, Italy) was set at an initial minimum speed of 2 rpm to reach the maximum speed of 80 rpm within 5 min. The whole test was performed in 3 consecutive days, and on each day, there were 3 test trials. Before the formal test, an acclimation session was performed using 2 rpm velocity for 1 min. The time the mouse fell down from the rod was recorded and was averaged across 3 trials.

Vertical climbing test. The experiment apparatus consists of a vertically placed rod (70 cm height, 1 cm diameter). At the beginning of each session, the mouse was placed on the top and was allowed to climb down to the bottom. There were 3 trials on each day, with 5-min interval between each trial. The whole test session lasted for 3 consecutive days.

Horizontal beam walking test. The experiment was performed using a wooden plate with 3 cm width and 70 cm length, with an escape box at one end of the beam. The whole apparatus was placed 100 cm above the ground. The mouse was placed at the end of the beam, and the time it took to reach the escape box was recorded. A total of 3 test trials were performed each day, with 5-min intervals. The whole test session lasted for 3 consecutive days.

Immunofluorescent staining
Mice were treated with 1.25% Avertin for anesthesia, followed by cardiac perfusion using 0.9% saline and 4% paraformaldehyde solution (PFA). The whole brain tissue was carefully removed and was fixed overnight using 4% PFA. The brain tissue was subsequently immersed in a 30% sucrose solution for 1–2 days of dehydration. The whole brain tissue was then cut into 40 μm using a sliding microtome (Lecia, Germany). After PBS washing and blocking, the brain slices were incubated with primary antibody at 4 °C for 48 h, followed by secondary antibody (see Supplementary Table 2 for antibody information). Images were captured with a confocal microscope (ZEISS, Germany).

Western blotting
Tissue lysates were extracted from the primary motor cortex, using the RIPA buffer (Thermo Scientific, US) containing protease and phosphatase inhibitors. After quantification using Pierce Rapid Gold BCA kit (Thermo Scientific, US), 25 μg protein samples were electrophoresed on 8% SDS-polyacrylamide gel and were transferred to the 0.2 μm PVDF membranes under 280 mA for 120 min. The membrane was washed by the TBST and blocked by 5% BSA and was incubated with primary antibody at 4 °C for 8 h. The membrane was then washed and incubated in a secondary antibody for 2 h (Supplementary Table 2). Images were captured by a protein imaging system (Bio-Rad, US) and the integrated gray values were calculated by ImageJ (NIH, US).

RT-qPCR
Total RNA was extracted from the primary motor cortex with Trizol (Invitrogen, US) reagent. Total RNA was reversely transcribed using Pre-script RT reagent Kit with gDNA Eraser (Takara, Japan). Real-time PCR was performed using SYBR Green reagent (Takara, Japan) and specific primers (see Supplementary Table 3).

Whole-cell patch-clamp recording
The mouse was deeply anesthetized with isoflurane, and coronal sections (250 μm thick) containing the primary motor cortex were prepared using a vibratome (VT1200S; Leica Microsystems, Germany) in ice-cold artificial cerebrospinal fluid (aCSF: 119 mM NaCl; 2.5 mM $CaCl_2$, 2.5 mM KCl, 1.3 mM $MgCl_2$, 1 mM NaH_2PO_4, 11 mM glucose, 26.2 mM $NaHCO_3$,

1.3 mM MgCl$_2$, and 290 mM mOsm, pH 7.4). The brain slices were recovered for 1 h at room temperature in aCSF. Slices were then transferred to the recording chamber with continuous perfusion of oxygenated aCSF containing 1 μM tetrodotoxin.

The whole-cell recording was performed on cortical L5 PNs using an epifluorescence microscope (Olympus, Japan). A glass pipette (WPI, US) was filled with internal solutions (135 mM CsMeSO$_3$, 8 mM NaCl, 10 mM Na$_2$-phosphocreatine, 0.25 mM EGTA, 2.17 mM Mg–adenosine 5′-triphosphate, 0.34 mM Na$_3$–guanosine 5′-triphosphate, and 10 mM HEPES (pH 7.4) with CsOH). The miniature excitatory postsynaptic currents (mEPSCs) were recorded using 1 μM TTX and 20 μM bicuculline. The miniature inhibitory postsynaptic currents (mIPSCs) were recorded using 1 μM TTX, 20 μM NBQX and 50 μM D-AP5. All recordings were performed using a Multiclamp 700B amplifier (Molecular Devices, US). Traces were low-pass-filtered at 2 kHz and digitized at 10 kHz. The pipette resistance ranged from 4 to 6 MΩ. During the recording, series resistance (Rs) was maintained between 10–20 MΩ. If Rs changed >20%, the data were excluded. Offline data analysis was performed using Clampfit 10.0 software (Molecular Devices, US).

Fiber photometry
In brief, at 2 weeks after AAV2/9- GCaMP6s virus injection, an optical fiber [OD = 230 mm, numerical aperture = 0.37] was inserted towards the dorsolateral striatum (AP: +0.6 mm, ML: ±2.4 mm, DV: −0.3 mm). The fiber was fixed with a skull penetrating screw and dental acrylic. Mice were then individually housed for 1-week recovery. The fluorescence signals were detected through the optic fiber using a fiber photometry system (Thinker Biotech, China). The 410 nm signal and 470 nm signal were recorded at the same time, while the 410 nm channel was used to correct for false positive signals from animal movement and bleaching. The values of fluorescence change (ΔF/F) were calculated as $(F − F_0) / F_0$, where F_0 was the averaged baseline fluorescence signal.

Statistics and reproducibility
GraphPad Prism 9.5 (GraphPad, US) was used for statistical analysis and data plotting. All data were plotted as mean ± SEM. Unpaired Student's *t*-test was used for comparing the means between two groups in two-tailed manners. For 2 independent variables, 2-way analysis of variance (ANOVA) and Sidak post hoc comparison were adopted. A significant level was defined when $P < 0.05$. The sample size of each experiment was reported in the relevant figure captions. No replicate was performed in most of the studies, except in those of qPCR, in which 3 replicates were performed for each sample.

Data availability
The RNA sequencing data has been deposited into the SRA database (Accession number: PRJNA1155630). All other datasets used for generating the figures are included in Supplementary Data 1.

References
1. Goedert, M. NEURODEGENERATION. Alzheimer's and Parkinson's diseases: the prion concept in relation to assembled Aβ, tau, and α-synuclein. *Science* **349**, 1255555 (2015).
2. Morris, H. R., Spillantini, M. G., Sue, C. M. & Williams-Gray, C. H. The pathogenesis of Parkinson's disease. *Lancet* **403**, 293–304 (2024).
3. Vázquez-Vélez, G. E. & Zoghbi, H. Y. Parkinson's disease genetics and pathophysiology. *Annu. Rev. Neurosci.* **44**, 87–108 (2021).
4. McGregor, M. M. & Nelson, A. B. Circuit mechanisms of Parkinson's disease. *Neuron* **101**, 1042–1056 (2019).
5. Roberts, R. F., Wade-Martins, R. & Alegre-Abarrategui, J. Direct visualization of alpha-synuclein oligomers reveals previously undetected pathology in Parkinson's disease brain. *Brain* **138**, 1642–1657 (2015).
6. Tanji, K. et al. Proteinase K-resistant α-synuclein is deposited in presynapses in human Lewy body disease and A53T α-synuclein transgenic mice. *Acta Neuropathol.* **120**, 145–154 (2010).
7. Muntané, G., Dalfó, E., Martinez, A. & Ferrer, I. Phosphorylation of tau and α-synuclein in synaptic-enriched fractions of the frontal cortex in Alzheimer's disease, and in Parkinson's disease and related α-synucleinopathies. *Neuroscience* **152**, 913–923 (2008).
8. Ren, J. X., Sun, X., Yan, X. L., Guo, Z. N. & Yang, Y. Ferroptosis in neurological diseases. *Front. Cell. Neurosci.* **14**, 218 (2020).
9. Mahoney-Sánchez, L. et al. Ferroptosis and its potential role in the physiopathology of Parkinson's disease. *Prog. Neurobiol.* **196**, 101890 (2021).
10. Stockwell, B. R. et al. Ferroptosis: a regulated cell death nexus linking metabolism, redox biology, and disease. *Cell* **171**, 273–285 (2017).
11. Lin, Z. H. et al. Quercetin protects against MPP$^+$/MPTP-induced dopaminergic neuron death in Parkinson's disease by inhibiting ferroptosis. *Oxid. Med. Cell. Longev.* **2022**, 7769355 (2022).
12. Anandhan, A. et al. α-Syn overexpression, NRF2 suppression, and enhanced ferroptosis create a vicious cycle of neuronal loss in Parkinson's disease. *Free Radic. Biol. Med.* **192**, 130–140 (2022).
13. Wang, Z. L., Yuan, L., Li, W. & Li, J. Y. Ferroptosis in Parkinson's disease: glia-neuron crosstalk. *Trends Mol. Med.* **28**, 258–269 (2022).
14. Ko, C. J., Gao, S. L., Lin, T. K., Chu, P. Y. & Lin, H. Y. Ferroptosis as a major factor and therapeutic target for neuroinflammation in Parkinson's disease. *Biomedicines* **9**, 1679 (2021).
15. Li, Y. et al. CXCL12 is involved in α-synuclein-triggered neuroinflammation of Parkinson's disease. *J. Neuroinflammation* **16**, 263 (2019).
16. Rajendran, L. & Paolicelli, R. C. Microglia-mediated synapse loss in Alzheimer's disease. *J. Neurosci.* **38**, 2911–2919 (2018).
17. Zabel, M. K. et al. Microglial phagocytosis and activation underlying photoreceptor degeneration is regulated by CX3CL1-CX3CR1 signaling in a mouse model of retinitis pigmentosa. *Glia* **64**, 1479–1491 (2016).
18. Sun, J. et al. Midbrain dopamine oxidation links ubiquitination of glutathione peroxidase 4 to ferroptosis of dopaminergic neurons. *J. Clin. Invest.* **133**, e165228 (2023).
19. Di Lazzaro, V. et al. Motor cortex hyperexcitability to transcranial magnetic stimulation in Alzheimer's disease. *J. Neurol. Neurosurg. Psychiatry* **75**, 555–559 (2004).
20. Ponzo, V. et al. Impaired intracortical transmission in G2019S leucine rich-repeat kinase Parkinson patients. *Mov. Disord.* **32**, 750–756 (2017).
21. Kreitzer, A. C. & Malenka, R. C. Striatal plasticity and basal ganglia circuit function. *Neuron* **60**, 543–554 (2008).
22. Chen, S. X., Kim, A. N., Peters, A. J. & Komiyama, T. Subtype-specific plasticity of inhibitory circuits in motor cortex during motor learning. *Nat. Neurosci.* **18**, 1109–1115 (2015).
23. Bartels, T., De Schepper, S. & Hong, S. Microglia modulate neurodegeneration in Alzheimer's and Parkinson's diseases. *Science* **370**, 66–69 (2020).
24. Dagher, N. N. et al. Colony-stimulating factor 1 receptor inhibition prevents microglial plaque association and improves cognition in 3xTg-AD mice. *J. Neuroinflammation* **12**, 139 (2015).
25. Hambright, W. S., Fonseca, R. S., Chen, L., Na, R. & Ran, Q. Ablation of ferroptosis regulator glutathione peroxidase 4 in forebrain neurons promotes cognitive impairment and neurodegeneration. *Redox Biol.* **12**, 8–17 (2017).
26. Miotto, G. et al. Insight into the mechanism of ferroptosis inhibition by ferrostatin-1. *Redox Biol.* **28**, 101328 (2020).
27. Taguchi, K., Watanabe, Y., Tsujimura, A. & Tanaka, M. Brain region-dependent differential expression of alpha-synuclein. *J. Comp. Neurol.* **524**, 1236–1258 (2016).
28. Taguchi, K. et al. Differential expression of alpha-synuclein in hippocampal neurons. *PLoS ONE* **9**, e89327 (2014).

29. Contractor, A., Ethell, I. M. & Portera-Cailliau, C. Cortical interneurons in autism. *Nat. Neurosci.* **24**, 1648–1659 (2021).
30. Lanoue, A. C., Blatt, G. J. & Soghomonian, J. J. Decreased parvalbumin mRNA expression in dorsolateral prefrontal cortex in Parkinson's disease. *Brain Res.* **1531**, 37–47 (2013).
31. Hijazi, S. et al. Early restoration of parvalbumin interneuron activity prevents memory loss and network hyperexcitability in a mouse model of Alzheimer's disease. *Mol. Psychiatry* **25**, 3380–3398 (2020).
32. Fu, Y. et al. Adaptive structural changes in the motor cortex and white matter in Parkinson's disease. *Acta Neuropathol.* **144**, 861–879 (2022).
33. Ruden, J. B., Dugan, L. L. & Konradi, C. Parvalbumin interneuron vulnerability and brain disorders. *Neuropsychopharmacology* **46**, 279–287 (2021).
34. Crapser, J. D. et al. Microglia facilitate loss of perineuronal nets in the Alzheimer's disease brain. *EBioMedicine* **58**, 102919 (2020).
35. Kvitsiani, D. et al. Distinct behavioural and network correlates of two interneuron types in prefrontal cortex. *Nature* **498**, 363–366 (2013).
36. Ferguson, B. R. & Gao, W. J. PV interneurons: critical regulators of E/I balance for prefrontal cortex-dependent behavior and psychiatric disorders. *Front. Neural Circuits* **12**, 37 (2018).
37. Zhang, C. et al. Dynamics of a disinhibitory prefrontal microcircuit in controlling social competition. *Neuron* **110**, 516–531.e516 (2022).
38. Gothner, T., Gonçalves, P. J., Sahani, M., Linden, J. F. & Hildebrandt, K. J. Sustained activation of PV+ interneurons in core auditory cortex enables robust divisive gain control for complex and naturalistic stimuli. *Cereb. Cortex* **31**, 2364–2381 (2021).
39. Khan, A. G. et al. Distinct learning-induced changes in stimulus selectivity and interactions of GABAergic interneuron classes in visual cortex. *Nat. Neurosci.* **21**, 851–859 (2018).
40. Yang, S. S., Mack, N. R., Shu, Y. & Gao, W. J. Prefrontal GABAergic interneurons gate long-range afferents to regulate prefrontal cortex-associated complex behaviors. *Front. Neural Circuits* **15**, 716408 (2021).
41. Mukherjee, A., Carvalho, F., Eliez, S. & Caroni, P. Long-lasting rescue of network and cognitive dysfunction in a genetic schizophrenia model. *Cell* **178**, 1387–1402.e1314 (2019).
42. Zhang, C. L. et al. Inhibitory control of synaptic signals preceding locomotion in mouse frontal cortex. *Cell Rep.* **37**, 110035 (2021).
43. Donato, F., Rompani, S. B. & Caroni, P. Parvalbumin-expressing basket-cell network plasticity induced by experience regulates adult learning. *Nature* **504**, 272–276 (2013).
44. Casula, E. P. et al. Low-frequency rTMS inhibitory effects in the primary motor cortex: insights from TMS-evoked potentials. *Neuroimage* **98**, 225–232 (2014).
45. Feng, Z. et al. Iron overload in the motor cortex induces neuronal ferroptosis following spinal cord injury. *Redox Biol.* **43**, 101984 (2021).
46. Duan, C. et al. Activation of the PPARγ prevents ferroptosis-induced neuronal loss in response to intracerebral hemorrhage through synergistic actions with the Nrf2. *Front. Pharmacol.* **13**, 869300 (2022).
47. Han, K. et al. Nrf2 knockout altered brain iron deposition and mitigated age-related motor dysfunction in aging mice. *Free Radic. Biol. Med.* **162**, 592–602 (2021).
48. Zhang, P. et al. Ferroptosis was more initial in cell death caused by iron overload and its underlying mechanism in Parkinson's disease. *Free Radic. Biol. Med.* **152**, 227–234 (2020).
49. Ryan, S. K. et al. Microglia ferroptosis is regulated by SEC24B and contributes to neurodegeneration. *Nat. Neurosci.* **26**, 12–26 (2023).
50. Zuo, Y. et al. Ferritinophagy-mediated ferroptosis involved in paraquat-induced neurotoxicity of dopaminergic neurons: implication for neurotoxicity in PD. *Oxid. Med. Cell. Longev.* **2021**, 9961628 (2021).
51. Zhang, N. et al. Ferritin confers protection against iron-mediated neurotoxicity and ferroptosis through iron chelating mechanisms in MPP+-induced MES23.5 dopaminergic cells. *Free Radic. Biol. Med.* **193**, 751–763 (2022).
52. Zhang, W. et al. Treadmill exercise relieves chronic restraint stress-induced cognitive impairments in mice via activating protein phosphatase 2A. *Neurosci. Bull.* **37**, 1487–1492 (2021).

Acknowledgements

Author contributions

B.Z., K.C., and L.Z. designed the whole experiment. B.Z. performed all experiments except electrophysiological studies. Y.D., X.L., Z.X. and W.Z. assisted in the execution and data analysis of behavioral, molecular, and histological assays, respectively. X.H. performed the patch-clamp recordings. This work was supervised by K.-F.S. and L.Z. The manuscript was prepared by B.Z. and L.Z., with inputs from all authors.

Competing interests

The authors declare no competing interests.

Additional information

Supplementary information The online version contains supplementary material available at https://doi.org/10.1038/s42003-024-06896-x.

Correspondence and requests for materials should be addressed to Li Zhang.

Peer review information *Communications Biology* thanks Bernard Schneider and the other anonymous reviewer(s) for their contribution to the peer review of this work. Primary handling editors: Christian Wozny, Anam Akhtar and Benjamin Bessieres.

Reprints and permissions information is available at http://www.nature.com/reprints

Publisher's note Springer Nature remains neutral with regard to jurisdictional claims in published maps and institutional affiliations.